The Astrophysical Journal, 952:117 (10pp), 2023 August 1 https://doi.org/10.3847/1538-4357/acda87

Solar Wind Modeling with the Alfvén Wave Solar atmosphere Model Driven by HMI-based Near-real-time Maps by the National Solar Observatory

Nishtha Sachdeva[1], Ward B. Manchester IV[1], Igor Sokolov[1], Zhenguang Huang[1], Alexander Pevtsov[2], Luca Bertello[2], Alexei A. Pevtsov[2], Gabor Toth[1], Bart van der Holst[1], and Carl J. Henney[3]
[1] Department of Climate and Space Sciences and Engineering, University of Michigan, Ann Arbor, MI 48109, USA; nishthas@umich.edu
[2] National Solar Observatory, 3665 Discovery Drive, 3rd Floor, Boulder, CO 80303, USA
[3] Air Force Research Laboratory, Space Vehicles Directorate, Kirtland AFB, NM 87117, USA
Received 2022 December 9; revised 2023 May 24; accepted 2023 May 26; published 2023 July 21

Abstract

We explore the performance of the Alfvén Wave Solar atmosphere Model with near-real-time (NRT) synoptic maps of the photospheric vector magnetic field. These maps, produced by assimilating data from the Helioseismic Magnetic Imager (HMI) on board the Solar Dynamics Observatory, use a different method developed at the National Solar Observatory (NSO) to provide a near contemporaneous source of data to drive numerical models. Here, we apply these NSO-HMI-NRT maps to simulate three full Carrington rotations: 2107.69 (centered on the 2011 March 7 20:12 CME event), 2123.5 (centered on 2012 May 11), and 2219.12 (centered on the 2019 July 2 solar eclipse), which together cover various activity levels for solar cycle 24. We show the simulation results, which reproduce both extreme ultraviolet emission from the low corona while simultaneously matching in situ observations at 1 au as well as quantify the total unsigned open magnetic flux from these maps.

Unified Astronomy Thesaurus concepts: Magnetogram (2359); Magnetohydrodynamics (1964); Magnetohydrodynamical simulations (1966); Solar wind (1534)

1. Introduction

Global estimates of the solar photospheric magnetic field in the form of synoptic and synchronic maps are the fundamental empirical data product that allow for simulation and prediction of the three-dimensional (3D) structure of the solar corona, solar wind, and the heliosphere (Mikic et al. 1999; Roussev et al. 2003; Usmanov & Goldstein 2003; Cohen et al. 2007; van der Holst et al. 2010, 2014, 2019; Lionello et al. 2013; Sokolov et al. 2013; Riley et al. 2014, 2019; Feng et al. 2014, 2015). These maps of the photospheric magnetic field are constructed from a time series of full-disk magnetograms (collected over a solar rotation period of 27 days or more), which are then modified and assembled to simultaneously cover the entire solar surface. Photospheric full-surface maps became available shortly following the routine production of full-disk magnetograms, beginning with the Global Oscillation Network Group (GONG) (see, e.g., Donaldson Hanna & Harvey 2002). The Stanford approach for producing synoptic maps from the Helioseismic Magnetic Imager (HMI) data is to use only 2° strips of data at the solar central meridian from each full-disk magnetogram and stitch these strips together to form synoptic maps.

Perhaps the most advanced system for producing global photospheric maps is the Air Force Data Assimilative Photospheric flux Transport (ADAPT) model, which is a flux transport model that makes use of data assimilation for incorporating magnetic field data. In ADAPT, the photospheric magnetic flux is transported by differential rotation, meridional flows, and convection-driven diffusion while observational data-driven updates to the model are made using data assimilation techniques (Arge et al. 2010, 2013; Hickmann et al. 2015; Schonfeld et al. 2022). ADAPT maps are routinely used in numerical simulations, including our work on model validation (Sachdeva et al. 2019, 2021) and simulations of Parker Solar Probe encounters (van der Holst et al. 2019, 2022) using the Alfvén Wave Solar atmosphere Model (AWSoM). Currently, the National Solar Observatory (NSO) provides ADAPT maps driven with GONG magnetograms (https://gong.nso.edu/adapt/maps/).

While the use of HMI and GONG informed ADAPT maps has been extremely successful, these data products are not suitable for use in near-real-time (NRT) simulations as a result of the significant time delay in producing the maps. For space weather forecasting, accurate maps with minimal delay from the moment the magnetic fields are observed are preferred. For this purpose, the National Solar Observatory embarked on a mission to produce NRT synoptic maps specifically designed as input for numerical models to forecast the coronal space environment. The synoptic map data products are available via Pevtsov & Bertello.[4]

The NSO approach is to speed map creation by using the full-disk vector magnetogram, and weight pixel contribution based on its distance from the central meridian (see, Bertello et al. 2014). The NRT synoptic maps (hereafter referred to as NSO-HMI-NRT) are a product of this NSO approach applied to HMI full-disk magnetograms. SOLIS/VSM vector data may also be used for NRT maps. While HMI and SOLIS/VSM produce different results for very weak fields and sometimes show the opposite orientation in transverse fields (Pevtsov et al. 2021b; Liu et al. 2022), the two instruments agree very well in strong field regions (Pietarila et al. 2013; Riley et al. 2014). The disagreement in weak magnetic field regions is not the result of disambiguation, but mostly due to differences in noise levels and magnetic fill factor (fraction of magnetized and

[4] https://doi.org/10.25668/nw0t-b078

non-magnetized plasma contribution to a single pixel) (Pevtsov et al. 2021b).

In this work, we explore the performance of AWSoM driven with NSO-HMI-NRT maps. For this goal, we choose three Carrington rotations (CRs): 2107 and 2108 (centered on 2011 March 7 20:12 UT, a CME event), 2123 (integer CR), and 2218–2219 (centered on 2019 July 2, total solar eclipse), which cover the ascending phase, solar maximum, and solar minimum of the solar cycle. For simplicity, hereafter we refer to these synoptic maps using their nearest integer rotation number (i.e., CR2107, CR2123, and CR2219) although two of them straddle more than one CR. We then make direct comparisons to observed data to provide a measure of model fidelity, first for coronal images made in the extreme ultraviolet, and second with in situ time series data extracted near Earth. For previous AWSoM model validation efforts using GONG and ADAPT magnetic field data products see Cohen et al. (2007), Jin et al. (2012), and Sachdeva et al. (2019, 2021). In Sections 2 and 3, we briefly describe the AWSoM model and the NSO-HMI-NRT maps while Section 4 describes the simulation design. Sections 5 and 6 describe simulation results and summarize this work.

2. AWSoM

AWSoM (Sokolov et al. 2013; van der Holst et al. 2014) within the Space Weather Modeling Framework (SWMF; Tóth et al. 2012) is a self-consistent, 3D global magnetohydrodynamic (MHD) model with its inner boundary at the base of the transition region (upper chromosphere) extending into the solar corona and the heliosphere. It is driven by the radial component of the photospheric magnetic field at the inner boundary. Like most solar corona models, this input comes from the solar synoptic/synchronic magnetic field maps, which is essential for reliable predictions. AWSoM incorporates the low-frequency Alfvén wave turbulence as a consequence of the nonlinear interaction of forward and counter-propagating Alfvén waves, which is based on well-established theories describing the evolution and transport of Alfvén turbulence, (e.g., Hollweg 1986; Matthaeus et al. 1999; Zank 2014; Zank et al. 2017). The AWSoM phenomenological approach self-consistently describes the heating and acceleration of the solar wind in response to turbulence while not yet including many higher-order physical effects. Several other extended MHD coronal models have been developed (Usmanov et al. 2000; Suzuki & Inutsuka 2005; Lionello et al. 2014), which also include Alfvén wave turbulence. AWSoM is distinguished from other global MHD models by including proton temperature anisotropy (perpendicular and parallel ion temperature), isotropic electron temperature, heat conduction, and radiative cooling. The wave dissipation heats the solar wind plasma and the (thermal and nonthermal) pressure gradients accelerate the solar wind (Meng et al. 2015). The full set of MHD equations using the Block Adaptive Tree Solarwind-Roe-Upwind Scheme (BATS-R-US; Powell et al. 1999) numerical scheme are solved within AWSoM. A detailed description of the model equations and their implementation is available in van der Holst et al. (2014). The energy partitioning scheme in AWSoM has been significantly improved and recently validated against the data from Parker Solar Probe (van der Holst et al. 2019, 2022). These improvements include using the critical balance formulation of Lithwick et al. (2007) and implementation of the alignment angle between the counter-propagating Alfvén waves in the energy cascade.

AWSoM has been meticulously validated by comparing the simulated results with a variety of observations. Near the Sun, the modeled density and temperature structure of the solar corona is compared to extreme ultraviolet (EUV) observations from the Solar-Terrestrial Relations Observatory (STEREO; Howard et al. 2008), Solar Dynamics Observatory (SDO; Pesnell et al. 2012)/Atmospheric Imaging Assembly (AIA; Lemen et al. 2012), and Solar and Heliospheric Observatory/Large Angle and Spectrometric Coronagraph (LASCO; Brueckner et al. 1995). In the low corona, AWSoM results have been compared with the tomographic reconstructions of electron density and temperature using EUV and visible-light observations (Lloveras et al. 2017, 2020, 2022; Vásquez et al. 2022). Within the radial distance range of $r \approx 1.055$–$6\ R_{\odot}$, AWSoM predicted electron density and temperature structure of the solar corona have excellent agreement (within ±20%–30%) with the 3D differential emission measure tomography reconstructions using EUV observations and rotational tomography with LASCO-C2 observations (Sachdeva et al. 2019). In the inner heliosphere, AWSoM quantitatively reproduces the tomographic reconstruction of the solar wind speed from the InterPlanetary Scintillation data (Jackson et al. 1998) between 100 $R_{\odot}$ and 1 au and the solar wind plasma parameters at 1 au (WIND observations) for two CRs near the end of solar cycle 24 (see Sachdeva et al. 2019 for detailed validation study).

3. NSO-HMI-NRT Maps

Here, we discuss the methodology of creating the NSO-HMI-NRT maps used in this paper for prescribing the magnetic field at the AWSoM inner boundary. Synoptic maps are constructed over a full solar rotation by adding new observations of the solar disk as they rotate into the observer's view. Assuming that the Sun rotates as a solid body, the synoptic maps cover the entire solar surface over a whole CR (∼27.27 days) (for a general description see, e.g., Pevtsov et al. 2021a, Section 7). Synoptic charts are created for each of the three components of the vector magnetic field: the B_r (radial, or up-down), B_{φ} (zonal, East-West), and B_{θ} (meridional, north–south). In addition, the synoptic charts also include maps of an average parameter that represents a *goodness* of disambiguation. In this paper, we limit our discussion to the synoptic charts representing the full vector magnetic field and do not discuss this parameter.

Various factors contribute to uncertainties in the synoptic charts. Posing the largest challenge are the limited contemporaneous observations of the solar surface, particularly in the polar regions. Instrumental noise, conditions of observations, and similar factors are also inherited in the maps. Smearing of solar features due to differential rotation is also a potential issue, particularly when creating high-spatial resolution synoptic maps. Because the differential component of solar rotation increases with latitude, the smearing effect will mostly be prominent within the polar regions (above 60°). A detailed description of this problem and a possible solution is given in Ulrich & Boyden (2006). However, due to the low resolution of the synoptic maps used in this study, this correction is not required.

As a first step in the creation of a synoptic map, full-disk images are remapped from sky-plane coordinates to heliographic coordinates. If remapping is required, the image

resolution is reduced to match the resolution of the synoptic map (e.g., $1^\circ \times 1^\circ$ in solar latitude and longitude). Next, these sampled or remapped images are added to a synoptic map based on heliographic coordinates of pixels. One method used by SDO/HMI team employs vertical strips of about 2 solar degrees wide centered at the solar central meridian. It produces the so-called diachronic maps. This method is quick and easy since it does not require excessive additional processing. However, it requires sufficiently high cadence in observations as the strips are simply added one after the other, similar to a picket fence. Therefore, any gap in observations results in a gap in the diachronic map. Furthermore, such a map fails to correctly represent any features that emerge or drastically evolve after passing the central meridian.

The NSO-HMI-NRT synoptic maps used in this paper are generated using a different approach that incorporates the use of the full-disk SDO/HMI magnetograms to build a synoptic map (e.g., Bertello et al. 2014). This method can be computationally expensive if the cadence of full-disk magnetograms is too high. However, the maps created with this technique include all the magnetic features regardless of when they appear during a rotation or whether they evolve significantly before and/or after passing the central meridian. Each NSO-HMI-NRT magnetic field map in this paper incorporates approximately 43 (8+27+8) days of observations. That is, in addition to the 27 days of a CR, the synoptic maps cover 8 days (each) before and after the rotation. While adding 8 days before/after the start/end of a CR is not necessary, it allows for a better equalization of weight (or number of contributing full-disk observations) for each heliographic pixel. Without this contribution, the first (last) 8 days of a CR map will see a gradual increase (decrease) in a normalized number of contributing points from just a few percent at the leading (trailing) edge to 100% in the center of the map. Because of this difference in weights, without additional 8 days, the noise level statistical variance would be slightly higher for the beginning and end parts of each map. As a rough estimate, when using additional 7 days instead of 8 days, a small range of longitudes near the synoptic map edge would undergo an increase in variance of about 10%. A similar procedure is adopted in creating the synoptic maps of pseudo-radial field using GONG observations. Our past experience with HMI vector observations has shown that the observation on the 48th minute of every hour provides the best coverage and data quality for the 1 h cadence that is used here. The selection of the 48th minute is not critical, and has minimal impact on the results of our project. Nevertheless, it may yield synoptic maps of slightly better quality.

The SDO/HMI data is acquired from the Joint Science Operations Center (JSOC; http://jsoc.stanford.edu/). This process begins by using a custom python program utilizing an http get request to the JSOC server to query the data that is available for download at that given time. This request is used to verify and record the availability status of all five Data Record Management System (DRMS) segments per observation that can be used to build a given synoptic map. Within JSOC these segments are identified as field, inclination, azimuth, disambig, and conf_disambig (map of the confidence in each pixels disambiguation) for the Full-Disk Milne-Eddington inversion data series (hmi.B_720s), each covering 720 s of observation. A 1 h cadence or five segments per hour are used to generate a synoptic map. If all five DRMS segments are available, they are separated into five lots of up to 9 days of data or $9 \times 24 \times 5 = 1080$ segments each. However, full block availability is rare and usually a few gaps of missing data occur every few days. Even with these gaps, this sums up to about 70 GB of observational data (before processing). This large amount of data requires parallelized workloads of each lot to reduce the computational time needed for the next steps. The data acquisition is followed by preprocessing of the SDO/HMI images of the photospheric magnetic field into a single coordinate system transformed package.

Preprocessing includes the coordinate transformation from the image (sky) plane to heliographic (solar latitude–longitude) coordinates, reimaging the full-disk data to larger pixels used for construction of a synoptic map, and applying $\cos^4$ of central meridian distance weighting function. For additional details see Bertello et al. (2014) and Hughes et al. (2016). After the preprocessing, the data are used to assemble a complete synoptic map by averaging the contribution to a corresponding synoptic map pixel from all contributing preprocessed images.

A well-known problem in constructing a full-surface synoptic map is the limited visibility of the polar fields of the Sun from near Earth. The Earth's heliographic latitude varies between $\pm 7.25^\circ$ each year, due to the tilt between the Earth's ecliptic plane and the solar rotation axis. The poles can therefore only be observed from the ecliptic plane with a large ($>80^\circ$) viewing angle. Moreover, each pole is not observable from near Earth for more than 6 months in a year. The unobserved polar fields are therefore required to be modeled. A simple approach, adopted here, is to fill the pixels corresponding to the unobserved polar data using a cubic surface fit to the observational data from the neighboring latitudes. Numerous studies suggest that the polar fields are approximately radially directed (Svalgaard et al. 1978; Petrie 2015). Ulrich & Tran (2013) used Mt. Wilson Observatory data to argue for a slight $\approx 6^\circ$ poleward inclination of the magnetic field in polar areas. Pevtsov et al. (2021a) applied a similar technique, and found about 3° equatorward inclination when using SOLIS/VSM data. Virtanen et al. (2019) also found a small ($\leqslant 10^\circ$) equatorward inclination at high ($\sim 75^\circ$) latitudes. Based on the results of these previous studies, we set the unobserved B_θ and B_ϕ values in the polar regions to zero and fill B_r using cubic surface fit. Finally, this process provides a complete synoptic map.

4. Numerical Simulation Setup

We use the NSO-HMI-NRT magnetic field maps for three CRs to drive the background solar wind simulations. The solar corona (SC) and inner heliosphere (IH) components of the SWMF are used via AWSoM (Section 2). The NSO-HMI-NRT synoptic maps used this in the study of CR2107 (2011 February 16 to 2011 March 16), CR2123 (2012 April 28 to 2012 May 25), and CR2219 (2019 June 29 to 2019 July 26) are shown in panels (a)–(c) of Figure 1. Each of these maps shows the structure of the photospheric magnetic field obtained from the SDO/HMI images followed by the procedure described in the previous Section 3. We include the GONG magnetogram and ADAPT-HMI map for CR2123 in panels (d) and (e) of Figure 1, respectively, which are also used in this study. In a previous work, Jin et al. (2017) used the GONG synoptic magnetogram to simulate the solar wind conditions for CR2107 using AWSoM for modeling a CME. van der Holst et al. (2014) and Meng et al. (2015) showed the solar wind model

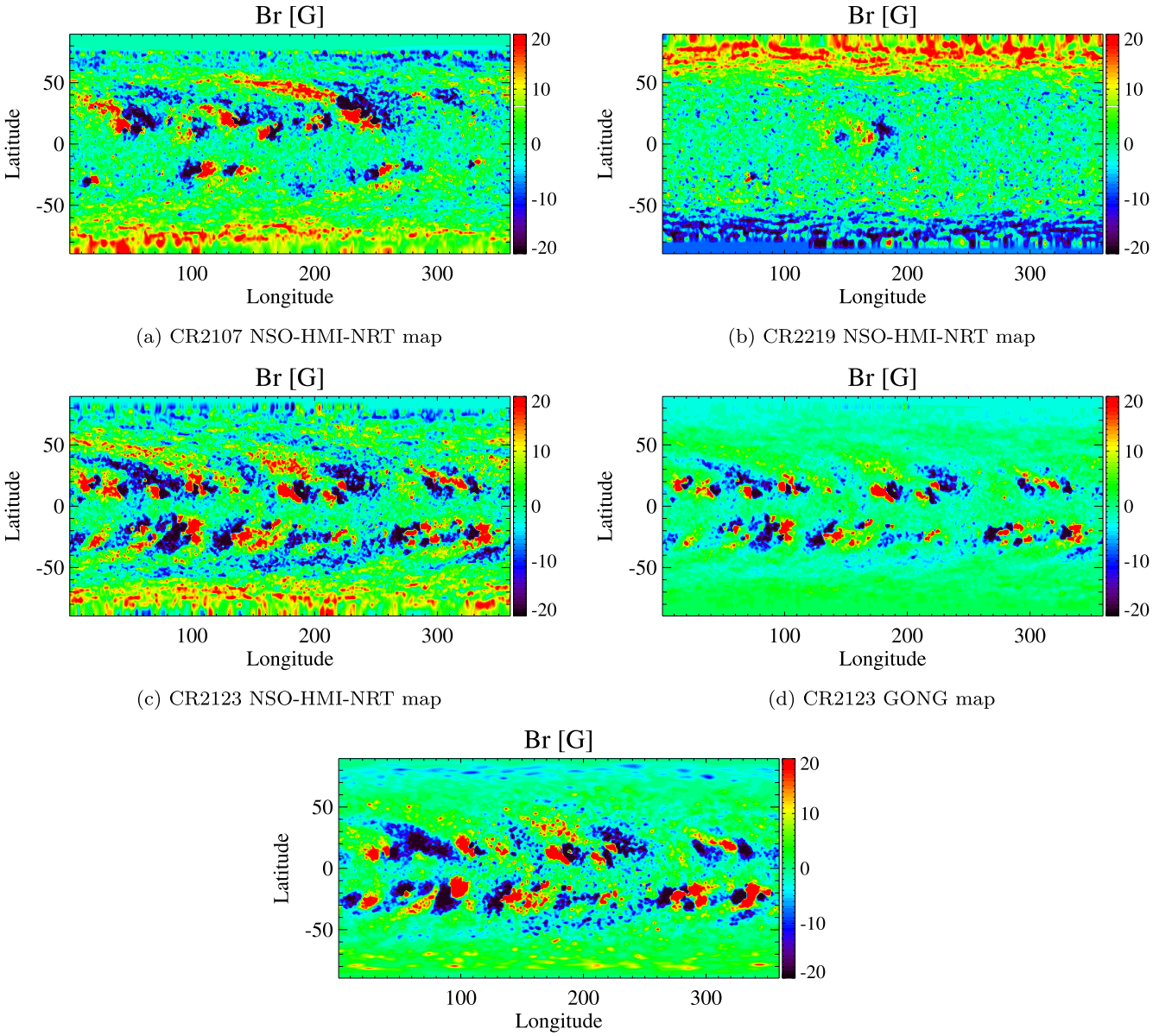

(a) CR2107 NSO-HMI-NRT map

(b) CR2219 NSO-HMI-NRT map

(c) CR2123 NSO-HMI-NRT map

(d) CR2123 GONG map

(e) CR2123 ADAPT-HMI map

Figure 1. NSO-HMI-NRT, ADAPT-HMI, and GONG synoptic maps showing the observed radial photospheric magnetic field. The B_r component from the NSO-HMI-NRT maps is shown for CR2107 and CR2219, and CR2123 in panels (a)–(c) respectively. Panels (d) and (e) show the B_r field from GONG synoptic map and ADAPT-HMI map respectively, for CR2123. The B_r field range of ± 20 G is chosen to highlight the features on the map.

results for this rotation using the magnetic field obtained from SDO/HMI instrument (Scherrer et al. 2012).

The 2D photospheric magnetic field from the synoptic maps is used to reconstruct the 3D magnetic field using the potential field source surface model (PFSSM; Schatten et al. 1969; Tóth et al. 2011). The radial component of the observed magnetic field is used as the boundary condition for the potential solver while the longitudinal and latitudinal components are allowed to relax to a solution. We use the spherical harmonics solution for the PFSSM with the source surface at 2.5 $R_\odot$ (Tóth et al. 2011). At the inner boundary, the initial temperature for both isotropic electron and perpendicular and parallel proton temperature is set to 50,000 K. The proton number density at these temperatures is overestimated to provide a ready source to replenish the plasma, which may be depleted due to chromospheric evaporation (Lionello et al. 2009; van der Holst et al. 2014). AWSoM has a limited number of free parameters that may be varied to improve the results when compared to observations of the solar wind. The energy density of the outward propagating Alfvén waves is set using the Poynting flux (S_A) of the wave which is proportional to the magnetic field strength at the inner boundary ($B_\odot$) (Fisk et al. 1999; Fisk 2001; Sokolov et al. 2013). A recent study by Huang et al. (2023) using AWSoM showed that the quantity $(S_A/B)_\odot$ needs to be varied based on the phase of the solar cycle. During phases of stronger magnetic activity, the amount of energy of the outward propagating Alfvén wave is reduced by reducing the $(S_A/B)_\odot$ parameter to avoid deposition of excess energy density into the chromosphere and high-density peaks at 1 au (Sachdeva et al. 2021). For CR2107, CR2123, and CR2219 the optimal value of the $(S_A/B)_\odot$ parameter in the model is set to 0.35, 0.3, and 1.0 in units of 10^6 Wm^{-2} T^{-1}, respectively. The

Alfvén wave correlation length ($L_\perp$), which is transverse to the magnetic field direction is proportional to $B^{-1/2}$ (Hollweg 1986) and is set to 1.5×10^5 m $\sqrt{T}$.

The SC component uses a 3D spherical grid extending from 1–24 $R_\odot$ (see, Figure 5 in van der Holst et al. 2010) and is coupled with the IH component, which uses a Cartesian grid that extends from −250 to 250 $R_\odot$ (Tóth et al. 2012). The SC and IH components are coupled with a buffer grid extending from 18–21 $R_\odot$ to transfer the SC solution to the IH domain in the steady-state run. The SC domain is decomposed into $6 \times 8 \times 8$ grid blocks while IH has $8 \times 8 \times 8$ grid blocks. The computation includes adaptive mesh refinement (AMR) in SC, which provides an angular resolution of 1.4° below 1.7 $R_\odot$ and 2.8° in the remaining domain. The number of cells in SC and IH is 4.2 million and 12.2 million, respectively. The cell size in IH ranges between 0.48 and 7.8 $R_\odot$. Using local time stepping, the SC component is run for 80,000 iterations and coupled with IH for one step followed by 5000 steps in IH to get the steady-state solution. Additional AMR is done below 1.7 $R_\odot$ along with the fifth-order shock-capturing scheme (Chen et al. 2016) to produce high-resolution line-of-sight synthetic EUV images for comparison with observations.

5. Results

We use the magnetic field from the NSO-HMI-NRT maps to obtain steady-state solar wind solutions for three CRs, 2107, 2123, and 2219. Figure 1 shows the NSO-HMI-NRT synoptic maps depicting detailed features of the active regions as well as the polar regions as described in Section 3. These maps represent different phases of the solar cycle. CR2107 and CR2123 correspond to higher solar activity with a stronger magnetic field and more active regions in comparison to the solar minimum conditions found in CR2219. Panels (c) and (d) of Figure 1 show a comparison between the magnetic field maps from NSO-HMI-NRT (left) and GONG (right) for CR2123. More small-scale features are present in the NSO-HMI-NRT map as well as stronger magnetic fields in the active regions. In the GONG map, the polar magnetic fields are weaker and smoother, a distinct difference that will impact the speed of the modeled solar wind.

The simulation domain for AWSoM covers the low corona making it ideal to obtain synthetic EUV images that can be compared with corresponding observations. Figure 2 shows the synthetic line-of-sight images from the AWSoM simulation results compared with corresponding SDO/AIA observations in six wavelength channels (94, 171, 193, 131, 211, and 335 Å). Here, panels (a)–(c) show model-data comparisons for CR2107, CR2219, and CR2123, respectively, modeled using the NSO-HMI-NRT maps. The first and third rows of images in each panel show the model-synthesized AIA images and the second and fourth rows of images show the corresponding SDO/AIA observations. Panels (d) and (e) of Figure 2 show the same model-data comparison for CR2123 modeled using the GONG magnetogram and ADAPT-HMI map, respectively. The simulation results compare well with observations in matching the overall relative brightness and the location of the major active regions for the three rotations. This fact suggests that AWSoM can reproduce the 3D structure of the density and temperature in the low solar corona. The modeled coronal holes (CHs) appear to be darker in comparison to observations but match their location and extent. The solar CHs have small-scale, closed field line loops and magnetic flux that add to their brightness. The numerical simulation however lacks these small-scale features and the CHs appear darker in the synthetic images. Although the average brightness matches well in all channels, the bright active regions can best be seen accurately in the 193, 211, and 335 Å channels. For example, for CR2107 in SDO/AIA 193 Å the active region on the west limb (right) is reproduced in the modeled image. For CR2219 (panel (b)), during solar minimum, the model AIA images reproduce the bright region, which can be seen clearly approximately at the center of the observations in these wavelength channels. The major active region at the center of the disk in the panels for CR2123 is reproduced in the model synthetic images as well. For CR2123, synthetic AIA images obtained from driving the model using the NSO-HMI-NRT and GONG maps show major differences in the overall brightness of the active regions and the CHs. In particular, the modeled CH from the GONG-driven simulation appears to be much darker. Additional refinement of the grid with the AWSoM model can further improve model comparisons by producing brighter active regions (Shi et al. 2022).

To compare the simulated solar wind with in situ observations of plasma parameters at L1 we extract (from the 3D result) the model solution along the trajectory of Earth. Figure 3 shows the AWSoM output along the Earth's trajectory in red and the OMNI data in black for all three rotations. We see that overall, the model when driven by NSO-HMI-NRT maps successfully reproduces the observed solar wind plasma. For the three rotations studied in this work, the solar wind solution matches quite well with the observations for all quantities. In each of the plots for 1 au comparisons, the dashed line indicates the arrival of a corotating interaction region (CIR) and the cyan solid line indicates CME arrival. For CR2107, the model reproduced the CIR on 2011 March 1 closely matching the significant jump in the radial speed (U_r), proton density (N_p), ion temperature, and the absolute magnetic field (B). Another CIR is observed on 2011 March 11 (Wood et al. 2012), which arrives much later in the simulated solution. For both rotations that represent the near solar maximum phase (CR2107 and CR2123), the features of CIRs (enhancements in the solar wind speed, proton density, and temperature and the magnetic field increase) in the solar wind plasma parameters are well matched by the model solution. For example, with the NSO-HMI-NRT maps, the peak model speed is overestimated by about 11% for CR2107 and 23% (in contrast to 7% for the ADAPT-HMI map result and about 61% for the GONG map result) for CR2123. As a result of the higher speed, the CIR in both cases arrive slightly earlier in the model as compared to the observations. CR2219 is a period of reduced activity for which the model overestimates the solar wind speed and density. However, the CIR speed in the model matches well with the observations. To further quantify the model-data comparison, we calculate a distance measure *Dist* listed in each plot, which informs us of how well the model matches observations. Described in detail in Sachdeva et al. (2019), the quantity *Dist* is a measure of the distance between two curves independent of the coordinates. Smaller values indicate a better fit. For CR2107 and CR2123, we calculate *Dist* to quantify only the steady-state background solar wind and exclude time intervals where there are signatures of CME arrival while for CR2107, we exclude the time interval—2011 March 10 07:00 to 2011 March 12 07:00 and for CR2123, we exclude 2012 May 16 16:00–2012 May 18 22:00. For CR2219 since there are no CMEs reaching Earth, we calculate the quantity *Dist* over the

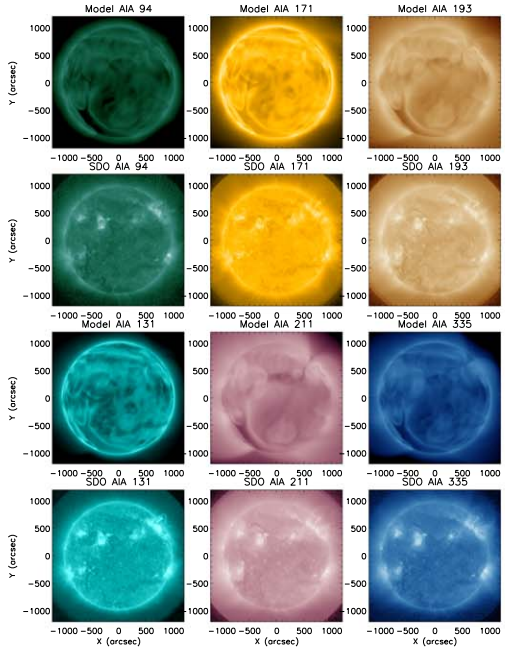

(a) CR2107 with NSO-HMI-NRT map

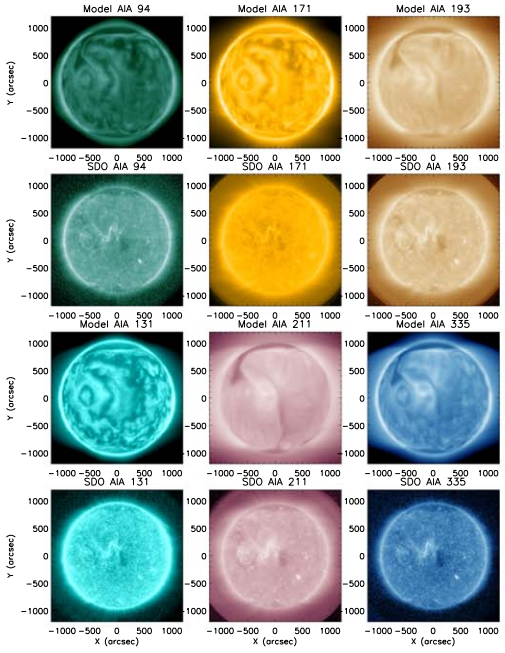

(b) CR2219 with NSO-HMI-NRT map

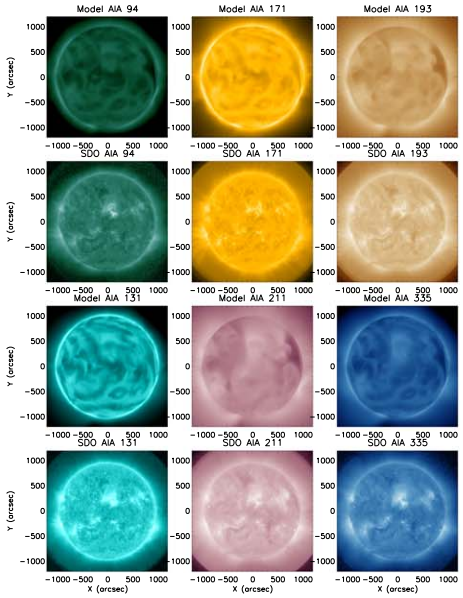

(c) CR2123 with NSO-HMI-NRT map

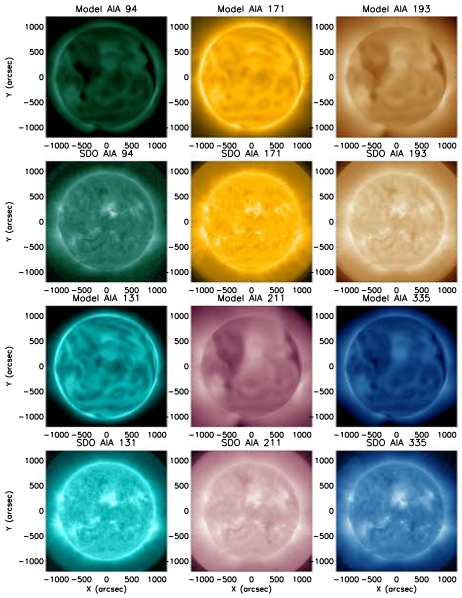

(d) CR2123 with GONG map

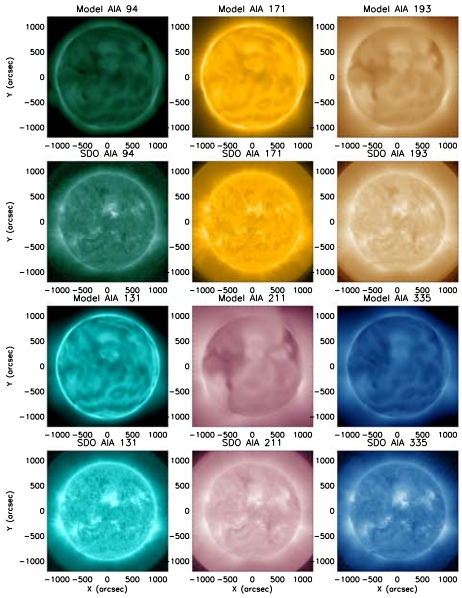

(e) CR2123 with ADAPT-HMI map

Figure 2. Comparison of synthetic EUV images with SDO/AIA observations. Panels (a)–(c) show the model-data comparison for CR2107, CR2219, and CR2123 modeled using the NSO-HMI-NRT maps. Panels (d) and (e) show the same for CR2123 modeled using the GONG magnetogram and ADAPT-HMI map, respectively. In each panel, the first and third rows represent the modeled AIA output and the second and fourth rows show the SDO/AIA observations. The comparison is shown in six wavelength channels (94, 171,193, 131, 211, and 335 Å).

entire rotation period. The modeled quantity B(nT) shown in the bottom row of these plots is the sum of the AWSoM background magnetic field strength (B) and the Alfvénic magnetic field fluctuations ($\sqrt{B^2 + \delta B^2}$, where δB is the magnitude of the magnetic field fluctuation (van der Holst et al. 2022). We see that the model sometimes underestimates the total magnetic field when compared to the hourly averaged magnetic field magnitude from OMNI data. This could be attributed to uncertainties associated with the input magnetograms due to the limited observations of the polar regions (Linker et al. 2017).

Panel (d) of Figure 3 shows the OMNI observations in black and the model results for CR2123 driven by NSO-HMI-NRT, GONG, and ADAPT-HMI maps (Panels (c)–(e) of Figure 1) are shown in red, blue, and pink, respectively. The modeled solutions differ significantly at 1 au, which is a direct result of the different initial magnetic field conditions from the two maps. All other model parameters are kept the same for both simulations. This demonstrates that the observational magnetic field input driving the solar corona models significantly impacts the solar wind properties. Figure 4 shows the comparison of AWSoM simulation results extracted along the trajectories of

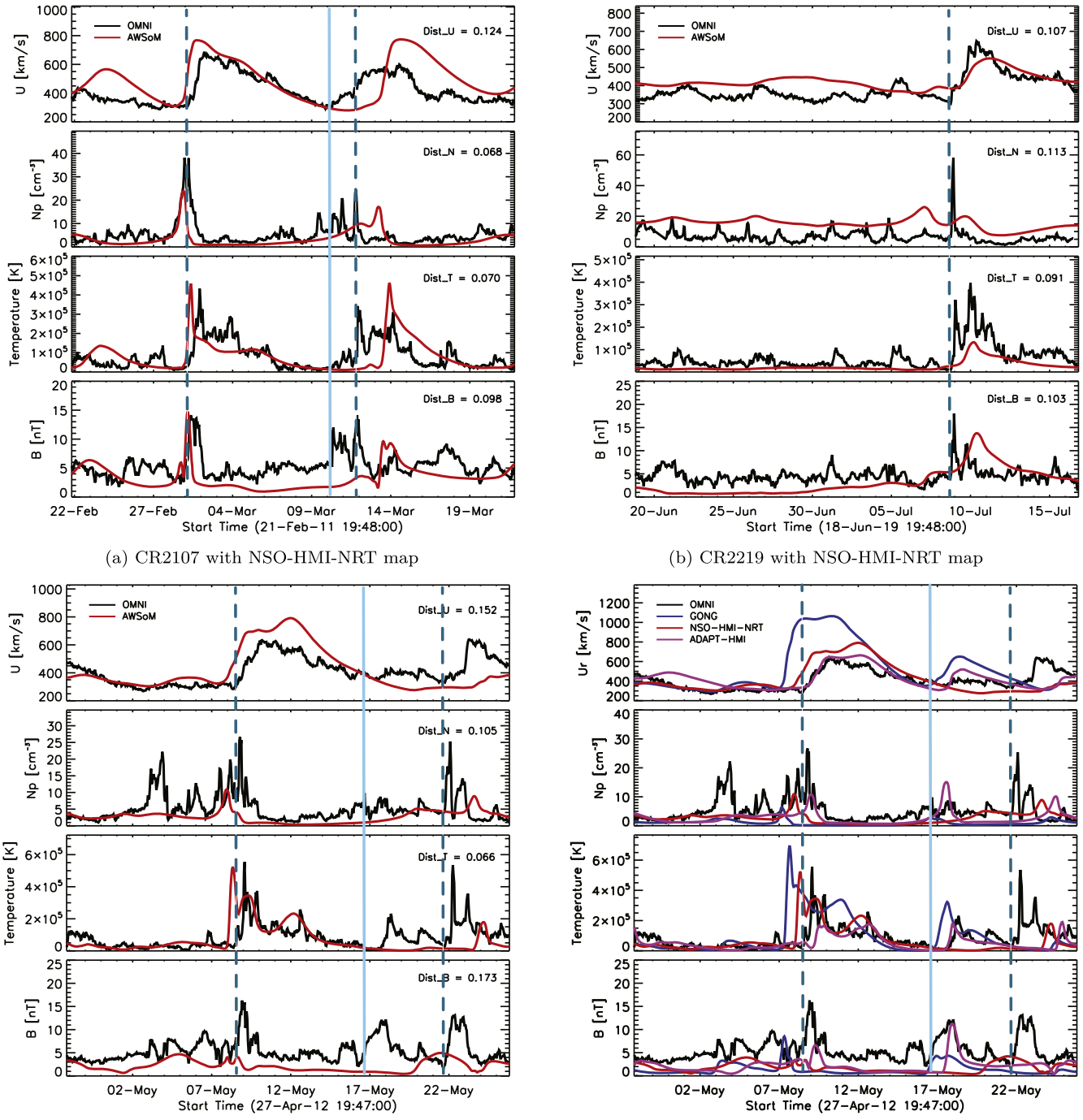

(a) CR2107 with NSO-HMI-NRT map

(b) CR2219 with NSO-HMI-NRT map

(c) CR2123 with NSO-HMI-NRT map

(d) CR2123 with GONG, NSO-HMI-NRT and ADAPT-HMI maps

Figure 3. Comparison of AWSoM simulated 1 au solar wind plasma parameters with the 1 h averaged OMNI observations for the three CRs. Model results are shown in red and data is in black. Panels (a)–(c) correspond to data-model comparisons for CR2107, CR2219, and CR2123, respectively, where the simulations were driven by the NSO-HMI-NRT maps (shown in Figure 1). Panel (d) shows the comparison of simulation results from AWSoM driven by the NSO-HMI-NRT (red), GONG (blue), and ADAPT-HMI (pink) maps (panels (c)–(e) in Figure 1) for CR2123. The dashed line indicates the arrival of a CIR and the cyan solid line indicates CME arrival.

STEREO-A (panel (a)) and STEREO-B (panel (b)) with observations. Three outputs are shown in red, blue, and pink from simulations driven by the NSO-HMI-NRT map, GONG map, and ADAPT-HMI map, respectively, for CR2123. Since there are multiple CMEs that hit these two instruments, in calculating *Dist* we exclude 2012 May 3 05:40 to 2012 May 4 05:40, 2012 May 18 17:17 to 2012 May 20 17:17 and 2012 May 23 23:00 to 2012 May 25 19:47 (end of the rotation) for STEREO-A. For STEREO-B, we exclude 2012 May 08 10:24 to 2012 May 11 09:47 and 2012 May 18 10:36 to 2012-0525 19:47. To further compare the modeled outputs using the NSO-HMI-NRT, GONG, and ADAPT-HMI maps for CR2123 with the solar wind plasma observations from OMNI, STEREO-A, and STEREO-B we list the quantity *Dist* for these comparisons in Tables 1–3, respectively.

Figure 5 represents the radial magnetic field (B_r) at the source surface radius of 2.5 $R_\odot$ obtained from the PFSSM

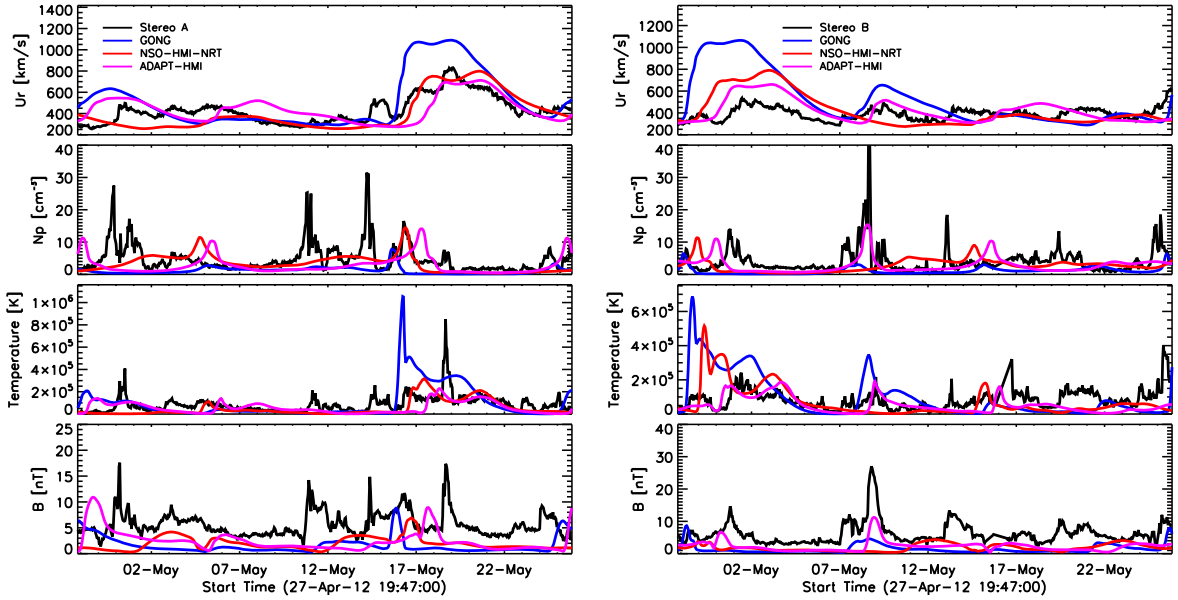

(a) CR2123 comparison for STEREO-A (b) CR2123 comparison for STEREO-B

Figure 4. Comparison of AWSoM simulated solar wind plasma parameters with the 1 h averaged STEREO-A/B observations for CR2123. Observations are in black. Panels (a) and (b) correspond to data-model comparisons for STEREO-A and B respectively. In each panel, the results shown are from AWSoM simulations driven by the NSO-HMI-NRT maps (red), GONG (blue), and ADAPT-HMI (pink) maps. These maps are shown in panels (c)–(e) of Figure 1.

Table 1
The Metric *Dist* for CR2123 Simulations Run with Three Different Input Magnetograms—NSO-HMI-NRT, GONG, and ADAPT-HMI Maps Compared with OMNI Observations

Input Map	Dist_*U*	Dist_*N*	Dist_*T*	Dist_*B*
NSO-HMI-NRT	0.152	0.105	0.066	0.173
GONG	0.239	0.161	0.112	0.172
ADAPT-HMI	0.090	0.113	0.086	0.158

Note. The quantity *Dist* is listed for each of the solar wind parameters, namely, U = speed, N = proton density, T = proton temperature, B = magnetic field.

Table 2
Same as Table 1 but for STEREO-A Observations

Input Map	Dist_*U*	Dist_*N*	Dist_*T*	Dist_*B*
NSO-HMI-NRT	0.098	0.111	0.068	0.175
GONG	0.122	0.149	0.113	0.180
ADAPT-HMI	0.100	0.135	0.067	0.155

using spherical harmonics with order 180 for each of the rotations. In panels (a)–(c), the field B_r is obtained from the NSO-HMI-NRT maps for CRs 2107, 2219, and 2123. For comparison, panels (d) and (e) show the B_r field obtained from the GONG map and ADAPT-HMI map for CR2123. All results for CR2123 (panels (c)–(e)) are shown on the same scale to highlight the differences between them. The field obtained from the NSO-HMI-NRT map is much more pronounced in the CHs as well as the polar regions in comparison to the GONG map.

To quantify this effect, we also calculate the total unsigned open magnetic flux for all the maps at 2.5 $R_\odot$. This quantity is an integral of the absolute value of the radial magnetic field, $|B_r|$, over the source surface. The total unsigned open magnetic flux at 2.5 $R_\odot$ is found to be 10.3, 15.9, and 6.9 [Gauss $R_\odot^2$] for the NSO-HMI-NRT maps for CR2107, CR2219, and CR2123,

Table 3
Same as Table 1 but for STEREO-B Observations

Input Map	Dist_*U*	Dist_*N*	Dist_*T*	Dist_*B*
NSO-HMI-NRT	0.205	0.060	0.144	0.126
GONG	0.336	0.057	0.221	0.131
ADAPT-HMI	0.140	0.046	0.100	0.120

respectively. For the GONG map for CR2123, the total unsigned magnetic flux obtained is 3.1 [Gauss $R_\odot^2$] at 2.5 $R_\odot$ and for the ADAPT-HMI map for CR2123 this quantity is 7.45 [Gauss $R_\odot^2$]. The scaling law by Pevtsov et al. (2003) relates the total unsigned flux to the energy deposition in the solar corona, therefore, a stronger total unsigned open flux leads to more energy, which accelerates and powers the solar wind. In relation to AWSoM, the Poynting flux outgoing into the solar wind is directly proportional to the unsigned open magnetic flux and the constant ratio of the Poynting flux to the magnetic flux is one of the input parameters of the model $(S_A/B)_\odot$. Therefore, the stronger open flux from the NSO-HMI-NRT map provides more energy to the corona, which increases chromospheric evaporation, increasing the density of the solar wind while reducing its speed. The result is a better comparison with observations at 1 au compared to the model results made with the GONG map for CR2123.

6. Summary and Discussion

In this work, we show the impact of the magnetic field conditions obtained from the NSO approach of creating NRT maps using the HMI magnetic field observations (NSO-HMI-NRT maps) on the modeled solar wind. The methodology used for these maps includes using a full-disk HMI magnetogram but with a weighted pixel contribution and the unobserved polar regions are filled using a polynomial fit to neighboring observations.

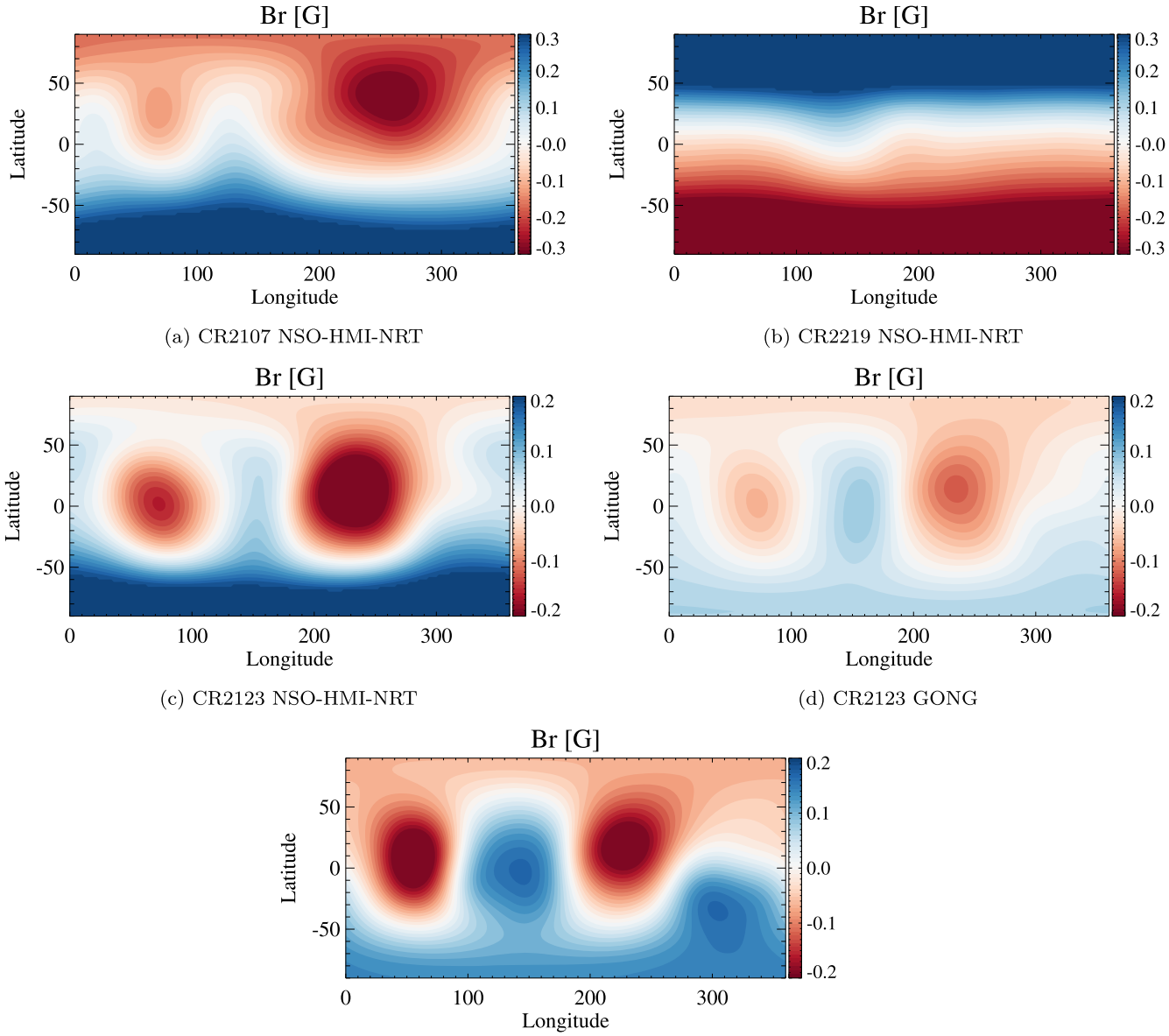

(a) CR2107 NSO-HMI-NRT

(b) CR2219 NSO-HMI-NRT

(c) CR2123 NSO-HMI-NRT

(d) CR2123 GONG

(e) CR2123 ADAPT-HMI

Figure 5. Radial magnetic field at the source surface radius (2.5 $R_\odot$). Panels (a)–(c) show the B_r magnetic field for CR2107, CR2219, and CR2123, respectively, at 2.5 $R_\odot$ calculated from the PFSSM using the NSO-HMI-NRT maps. Panels (d) and (e) show the same for CR2123 using the GONG synoptic map and ADAPT-HMI map. The source surface in the PFSSM is set to 2.5 $R_\odot$ for all the maps.

We use the 3D MHD model AWSoM to simulate the Sun-to-Earth background solar wind for three CRs (2107, 2219, and 2123). AWSoM is driven by the magnetic field from the NSO-HMI-NRT maps to demonstrate their performance during varying periods of solar activity. We compare the AWSoM simulated solar wind solutions with observations in the low corona and find that for all three CRs modeled using the corresponding NSO-HMI-NRT maps as input, the large-scale properties of the solar corona including the extent and location of CHs as well as regions of enhanced activity (active regions) compare well with SDO/AIA observations.

Further away from the Sun, we compare the observed solar wind properties at 1 au with the model results. The 1 au observations are reproduced reasonably well by the NSO-HMI-NRT map-driven AWSoM model for all three rotations. We find that while the magnetic field is systematically underestimated, the solar wind speed, density, and CIR properties are reproduced in the simulations. For one of the rotations (CR2123), we obtain the solar wind solution using the GONG synoptic map and ADAPT-HMI map as the initial condition for the photospheric magnetic field and compare the results with the NSO-HMI-NRT map-driven solar wind conditions. We find that the solutions with the NSO-HMI-NRT map perform well both in the low corona and at 1 au when compared to the GONG map results. Finally, we show the radial magnetic field at 2.5 $R_\odot$ from the PFSSM for each of the maps and compare the total unsigned open magnetic flux at the source surface. This quantity for the NSO-HMI-NRT map is larger by a factor of $\approx$2 in comparison to the GONG map for the same rotation but comparable to the ADAPT-HMI map solution.

It is well known that numerical models of the solar corona are sensitive to the observed magnetic field inputs obtained from a variety of synoptic magnetograms available in the community. Here, we highlight the performance of

NSO-produced, HMI observation-based, NRT (NSO-HMI-NRT) maps with our 3D extended MHD model (AWSoM) and show that the NSO-HMI-NRT maps are a valuable data product allowing for coronal/solar wind simulations of equal or better quality than those obtained by standard synoptic maps such as GONG maps.

Acknowledgments

This work was primarily funded by the NASA 80NSSC17K0686 grant, NASA LWS grant 80NSSC22K0892, and NSF grants PHY-2027555, 1663800, and ANSWERS grant GEO-2149771. W.M. was also supported by NASA LWS grant NNX16AL12G. I.S. was also supported by NSF-2149771. Z.H. was also supported by the NASA grant No. 80NSSC23K0450 and the NASA grant No. 80NSSC22K0269 as well.

Original full-disk magnetograms that were used to create synoptic maps are courtesy of NASA/SDO and the HMI science team. The NSO is operated by the Association of Universities for Research in Astronomy (AURA), Inc., under a cooperative agreement with the National Science Foundation. The ADAPT model development is supported by Air Force Research Laboratory (AFRL), along with AFOSR (Air Force Office of Scientific Research) tasks 18RVCOR126 and 22RVCOR012. This work utilizes data produced collaboratively between AFRL and the NSO. The views expressed are those of the authors and do not reflect the official guidance or position of the United States Government, the Department of Defense (DoD), or of the United States Air Force.

We acknowledge the high-performance computing support from (a) Cheyenne[5] provided by NCAR's Computational and Information Systems Laboratory, sponsored by the NSF, (b) Frontera[6] sponsored by the NSF, and (c) the NASA supercomputing system Pleiades[7] as part of the NASA High-End Computing (HEC) Program through the NASA Advanced Supercomputing (NAS) Division at Ames Research Center.

ORCID iDs

Nishtha Sachdeva https://orcid.org/0000-0001-9114-6133
Ward B. Manchester IV https://orcid.org/0000-0003-0472-9408
Igor Sokolov https://orcid.org/0000-0002-6118-0469
Zhenguang Huang https://orcid.org/0000-0003-1674-0647
Alexander Pevtsov https://orcid.org/0000-0001-9746-9937
Luca Bertello https://orcid.org/0000-0002-1155-7141
Alexei A. Pevtsov https://orcid.org/0000-0003-0489-0920
Gabor Toth https://orcid.org/0000-0001-8459-2100
Bart van der Holst https://orcid.org/0000-0001-5260-3944
Carl J. Henney https://orcid.org/0000-0002-6038-6369

References

Arge, C. N., Henney, C. J, Hernandez, I. G., et al. 2013, in AIP Conf. Proc. 1539, Solar Wind 13, ed. G. P. Zank et al. (Melville, NY: AIP), 11
Arge, C. N., Henney, C. J., Koller, J., et al. 2010, in AIP Conf. Proc. 1216, Twelfth Int. Solar Wind Conf., ed. M. Maksimovic et al. (Melville, NY: AIP), 343
Bertello, L., Pevtsov, A. A., Petrie, G. J. D., & Keys, D. 2014, SoPh, 289, 2419
Brueckner, G. E., Howard, R. A., Koomen, M. J., et al. 1995, SoPh, 162, 357
Chen, Y., Tóth, G., & Gombosi, T. I. 2016, JCoPh, 305, 604
Cohen, O., Sokolov, I., Roussev, I., et al. 2007, ApJ, 654, L163
Donaldson Hanna, K. L., & Harvey, J. W. 2002, AAS Meeting, 200, 04.03
Feng, X., Ma, X., & Xiang, C. 2015, JGRA, 120, 10159
Feng, X., Zhang, M., & Zhou, Y. 2014, ApJS, 214, 6
Fisk, L. A. 2001, JGR, 106, 15849
Fisk, L. A., Zurbuchen, T. H., & Schwadron, N. A. 1999, ApJ, 521, 868
Hickmann, K. S., Godinez, H. C., Henney, C. J., & Arge, C. N. 2015, SoPh, 290, 1105
Hollweg, J. V. 1986, JGR, 91, 4111
Howard, R. A., Moses, J. D., Vourlidas, A., et al. 2008, SSRv, 136, 67
Huang, Z., Tóth, G., Sachdeva, N., et al. 2023, ApJL, 946, L47
Hughes, A. L. H., Bertello, L., Marble, A. R., et al. 2016, arXiv:1605.03500
Jackson, B. V., Hick, P. L., Kojima, M., & Yokobe, A. 1998, JGR, 103, 12049
Jin, M., Manchester, W. B., van der Holst, B., et al. 2012, ApJ, 7745, 6
Jin, M., Manchester, W. B., van der Holst, B., et al. 2017, ApJ, 834, 173
Lemen, J. R., Title, A. M., Akin, D. J., et al. 2012, SoPh, 275, 17
Linker, J. A., Caplan, R. M., Downs, C., et al. 2017, ApJ, 848, 70
Lionello, R., Downs, C., Linker, J. A., et al. 2013, ApJ, 777, 76
Lionello, R., Linker, J. A., & Mikić, Z. 2009, ApJ, 690, 902
Lionello, R., Velli, M., Downs, C., et al. 2014, ApJ, 784, 120
Lithwick, Y., Goldreich, P., & Sridhar, S. 2007, ApJ, 655, 269
Liu, Y., Griñón-Marín, A. B., Hoeksema, J. T., Norton, A. A., & Sun, X. 2022, SoPh, 297, 17
Lloveras, D. G., Vásquez, A. M., Nuevo, F. A., et al. 2020, SoPh, 295, 76
Lloveras, D. G., Vásquez, A. M., Nuevo, F. A., et al. 2022, JGRA, 127, e30406
Lloveras, D. G., Vásquez, A. M., Nuevo, F. A., & Frazin, R. A. 2017, SoPh, 292, 153
Matthaeus, W. H., Zank, G. P., Oughton, S., Mullan, D. J., & Dmitruk, P. 1999, ApJL, 523, L93
Meng, X., van der Holst, B., Tóth, G., & Gombosi, T. I. 2015, MNRAS, 454, 3697
Mikic, Z., Linker, J., Schnack, D., Lionello, R., & Tarditi, A. 1999, PhPl, 6, 2217
Pesnell, W. D., Thompson, B. J., & Chamberlin, P. C. 2012, SoPh, 275, 3
Petrie, G. J. D. 2015, LRSP, 12, 5
Pevtsov, A. A., Bertello, L., Nagovitsyn, Y. A., Tlatov, A. G., & Pipin, V. V. 2021a, JSWSC, 11, 4
Pevtsov, A. A., Fisher, G. H., Acton, L. W., et al. 2003, ApJ, 598, 1387
Pevtsov, A. A., Liu, Y., Virtanen, I., et al. 2021b, JSWSC, 11, 14
Pietarila, A., Bertello, L., Harvey, J. W., & Pevtsov, A. A. 2013, SoPh, 282, 91
Powell, K., Roe, P., Linde, T., Gombosi, T., & De Zeeuw, D. L. 1999, JCoPh, 154, 284
Riley, P., Ben-Nun, M., Linker, J. A., et al. 2014, SoPh, 289, 769
Riley, P., Linker, J. A., Mikic, Z., et al. 2019, ApJ, 884, 18
Roussev, I., Gombosi, T., Sokolov, I., et al. 2003, ApJL, 595, L57
Sachdeva, N., Tóth, G., Manchester, W. B., et al. 2021, ApJ, 923, 176
Sachdeva, N., van der Holst, B., Manchester, W. B., et al. 2019, ApJ, 887, 83
Schatten, K. J., Wilcox, J. M., & Ness, N. F. 1969, SoPh, 6, 442
Scherrer, P. H., Schou, J., Bush, R. I., et al. 2012, SoPh, 275, 207
Schonfeld, S. J., Henney, C. J., Jones, S. I., & Arge, C. N. 2022, ApJ, 932, 115
Shi, T., Manchester, Ward, I., Landi, E., et al. 2022, ApJ, 928, 34
Sokolov, I. V., van der Holst, B., Oran, R., et al. 2013, ApJ, 764, 23
Suzuki, T. K., & Inutsuka, S.-I 2005, ApJL, 632, L49
Svalgaard, L., Duvall, T. L. J., & Scherrer, P. H. 1978, SoPh, 58, 225
Tóth, G., Meng, X., Gombosi, T. I., & Ridley, A. 2011, JGR, 116, A07211
Tóth, G., van der Holst, B., Sokolov, I. V., et al. 2012, JCoPh, 231, 870
Ulrich, R. K., & Boyden, J. E. 2006, SoPh, 235, 17
Ulrich, R. K., & Tran, T. 2013, ApJ, 768, 189
Usmanov, A. V., & Goldstein, M. L. 2003, JGR, 108, 1354
Usmanov, A. V., Goldstein, M. L., Besser, B. P., & Fritzer, J. M. 2000, JGR, 105, 12675
van der Holst, B., Huang, J., Sachdeva, N., et al. 2022, ApJ, 925, 146
van der Holst, B., Manchester, W., Frazin, R., et al. 2010, ApJ, 725, 1373
van der Holst, B., Manchester, W. B. I, Klein, K. G., & Kasper, J. C. 2019, ApJL, 872, L18
van der Holst, B., Sokolov, I., Meng, X., et al. 2014, ApJ, 782, 81
van der Holst, B., Sokolov, I. V., Meng, X., et al. 2014, ApJ, 782, 81
Vásquez, A. M., Nuevo, F. A., Frassati, F., et al. 2022, SoPh, 297, 120
Virtanen, I. I., Pevtsov, A. A., & Mursula, K. 2019, A&A, 624, A73
Wood, B. E., Wu, C. C., Rouillard, A. P., Howard, R. A., & Socker, D. G. 2012, ApJ, 755, 43
Zank, G. P. 2014, Transport Processes in Space Physics and Astrophysics, Vol. 877 (New York: Springer)
Zank, G. P., Adhikari, L., Hunana, P., et al. 2017, ApJ, 835, 147

[5] https://arc.ucar.edu/knowledge_base/70549542
[6] https://frontera-portal.tacc.utexas.edu
[7] https://www.nas.nasa.gov/hecc/resources/pleiades.html